Candidate Landing Sites for the Emirates Lunar Mission (ELM) Rashid-1 Rover

Jessica Flahaut, S. Els, M. Joulaud, C. Wöhler, S. Breton, Evelyn Füri, S. Almaeeni, H. Almarzooqi

Candidate landing sites for the Emirates Lunar Mission (ELM) Rashid-1 rover

J. Flahaut [1]*, S.G. Els[2], M. Joulaud[1,3], C. Wöhler[4], S. Breton[1], E. Füri[1], S. AlMaeeni[2], H. Almarzooqi[2] and the ELM Science Collaboration

[1]*Université de Lorraine, CNRS, CRPG, Nancy F-54000, France*

[2] *Mohammed Bin Rashid Space Centre (MBRSC), PO Box 211833, Dubai, United Arab Emirates*

[3] *Laboratoire de Géologie de Lyon : Terre, Planètes, Environnement (LGL-TPE), Université Claude Bernard Lyon1/CNRS/ENS, Villeurbanne F- 69622, France*

[4] *Image Analysis Group, TU Dortmund University, Otto-Hahn-Str. 4, 44227 Dortmund, Germany.*

* Corresponding Author, email: jessica.flahaut@univ-lorraine.fr

Keywords

Emirates Lunar Mission, Moon, landing site, lunar geology, Rashid-1 rover

Abstract

Launched in December 2022 onboard the Hakuto-R lunar lander, the Mohammed Bin Rashid Space Centre (MBRSC) Emirates Lunar Mission (ELM) Rashid-1 rover experienced an unsuccessful landing on the lunar surface on April 25th, 2023. The mission's prime landing site was Atlas crater, a 87 km diameter floor-fractured crater emplaced within the lunar highlands in the northeastern quadrant of the Moon. This paper describes the landing site selection procedure for the ELM Rashid-1 rover, from technical requirements that led to the selection of four broad areas of interest, to the placement of candidate landing ellipses based primarily on slope analysis and science interest. The rock abundance and presence of boulders were

analyzed to verify the suitability of the target location for landing. Geological context as well as high resolution imagery and topography are presented for the four selected landing sites: Atlas crater (prime), Sinus Iridum, Oceanus Procellarum, and Lacus Somniorum (back-ups). Terrain characteristics and key science questions to be addressed at these locations are discussed, emphasizing the high scientific value of these locations for future lunar missions.

1. Introduction

Selecting the landing site is a crucial element in the preparation of any planetary surface mission. The landing site selection shall ensure that the terrain properties allow for a safe landing and that the scientific goals of the mission can be achieved. This process requires a review and correlation of available data to identify the most suitable location using a mission specific metric (e.g., Flahaut et al., 2012, 2020; Kring and Durdas, 2012; Lemelin et al., 2014; Liu et al., 2021). Thanks to a number of lunar orbiters (e.g., Lunar Reconnaissance Orbiter (LRO), SELenological and ENgineeering Explorer (SELENE), Chandrayaan-1), the Moon's surface has been well-mapped, and an extensive amount of high-resolution remote sensing data has been assembled over the past two decades (e.g., Keller et al., 2016; Staid et al., 2011; Haruyama et al., 2008; Fortezzo et al., 2020). These data allow us to pursue a rigorous site selection scheme for upcoming lunar surface missions.

Over recent years, the lunar community's pursuit of returning to the surface of the Moon has gained a lot of momentum, and several entities aim to deploy experiments on the lunar surface. The *Rashid-1* lunar rover was the main component of the Emirates Lunar Mission (ELM) program, developed at the Mohammed Bin Rashid Space Center (MRSC) in Dubai. This 10 kg micro-rover was equipped with 4 imagers (including 2 wide angles cameras, 1 microscopic camera and 1 thermal camera), 4 Langmuir probes and a material adhesion experiment on its wheels. Although Rashid-1 was designed primarily as a technological demonstration, this set of scientific instruments and experiments would have allowed it to investigate lunar surface properties and processes, as well as testing of materials in support of future lunar missions (Almarzooqi and AlMaeeni, 2021; Els et al. 2021; Els et al., this issue). The Rashid-1 rover was transported to the lunar surface on-board the M1 mission (the Hakuto-R lander) of the commercial lunar delivery service provider ispace which experienced an unsuccessful landing in April 2023.

After an initial selection of landing site candidates (mainly based upon orbital and technical constraints of the M1 Mission), broad regions were further evaluated by the ELM Science Team in terms of topography and geology. This step narrowed down the possibilities to four candidate sites, which were considered suitable for landing and conducting the Rashid-1 surface mission. In this paper, we describe the process and method used to select the candidate landing sites, and we detail their terrain characteristics and geological context. In Section 2, we briefly discuss the pre-selection of the wider candidate areas and the technical criteria related to the mission. Section 3 outlines the methodologies to pin-point the best location for landing within these candidate areas. Section 4 provides an overview of the topographic and scientific features of the four selected locations, while in Section 5 cross-investigations that should have been carried out in situ with the rover are discussed.

2. Pre-selection constraints for the candidate areas

The selection process of the landing locations started with the pre-selection of regional areas for landing that complied with the prime technical constraints. These areas extend over several degrees in longitude and latitude. Within each of the resulting four areas, a candidate location – the so-called landing ellipse – was then identified. This landing ellipse represents the area of uncertainty of landing, and in our specific case, the ellipse has the geometry of a circle.

2.1 Latitudinal constraints

The primary mission requirement provided by ispace for the ELM and M1 was that the landing site should be located at mid-latitudes, within a band of 45 ± 7.5° latitude. To allow for direct communication with Earth, only the nearside of the Moon was to be considered. In the early project stage, both the northern and southern hemispheres were considered. However, the southern hemisphere, which is dominated by rough highland terrains, was ultimately rejected, and the detailed landing site search focused on the northern latitudes only.

2.2 Orbital constraints

In addition to identifying a prime landing site, several suitable back-up locations had to be selected. The prime and back-up sites are linked by the orbit of the lander spacecraft, as only locations which could be reached without major (or no) orbit correction could be considered

as back-up. Given that landing was to be achieved at a similar time after sunrise at the prime and back-up sites on the same lunar day, the ispace Mission Analysis group defined 'iso-solar points'; thus, if a landing opportunity was missed at one site, the next (back-up) site would be reached at a similar synodic time. The details of this definition will be described elsewhere (Yam et al., *in prep*.). This entails that once an area for the prime landing site was selected, the back-up locations were restricted to specific areas on the Moon. It should be noted that the iso-solar point does not strictly describe a point, but rather represents an area extending over a few degrees in longitude and latitude. This flexibility allowed us to select all sites (including back-up ones) primarily based on scientific rather than orbital constraints.

2.3 Selected Regional Search Areas

To further pinpoint possible areas for landing, which would be several hundreds of kilometers in size, lunar geological maps were investigated to first identify wider regions of high geologic diversity (e.g., Fortezzo et al., 2020). Attention was especially given to relatively flat mare areas, in proximity to highlands or other features of scientific interest (e.g., NRC, 2007; Flahaut et al., 2012, 2023a). Pre-selected broader regions initially included Sinus Iridum, Oceanus Procellarum, and Lacus Somniorum, the three maria attainable at the targeted latitudes (45° ± 7.5 °N). As Sinus Iridum and Oceanus Procellarum had already been explored by the Chang'E-3 and Chang'E-5 missions, respectively, the poorly known Lacus Somniorum area, which displays diverse geology (with at least four accessible mare and highland units within the landing region) was first anticipated to be the prime landing site (e.g., Flahaut et al., 2021). However, updated requirements from ispace to land at higher latitudes because of thermal constraints led us to investigate regions further to the north of Lacus Somniorum and to add western Frigoris (including Hercules and Atlas craters) to the candidate landing areas. Ultimately, to meet the new demands from ispace, the prime landing site was shifted to the interior of Atlas crater at the time of launch, in December 2022.

Further analyses of available high-resolution imagery and topographic data were then conducted to identify the best areas to fit an 8 km diameter landing ellipse (the geometry and maximum size of the landing area defined by ispace) with low slopes (<15°) and high scientific value within these four wider areas (see section 3).

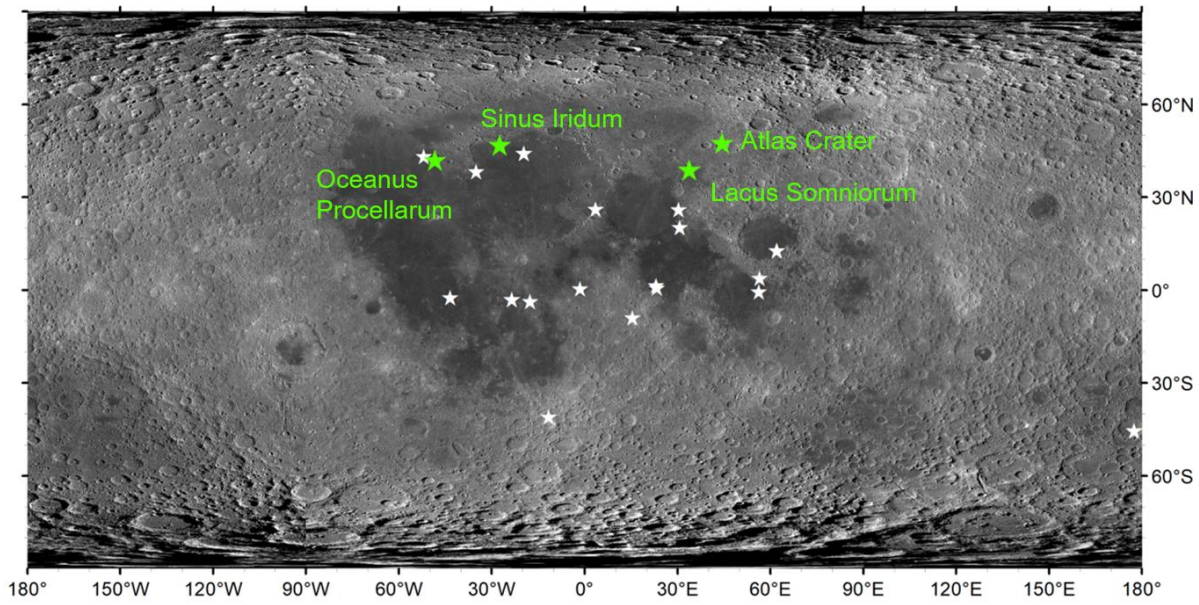

Figure 1: Location of the four ELM candidate landing sites (green stars) at 45 ± 7.5°N on the lunar nearside. White stars indicate the locations of the previous Surveyor, Apollo, Luna, and Chang'E lander missions.

3. Dataset and Methodology

3.1 Available Dataset

Available remote sensing datasets from past and ongoing lunar missions were downloaded from the NASA Planetary Data System (PDS) and JAXA's SELENE Archive, processed (e.g., calibrated, map-projected, mosaicked) and integrated into a Geographic Information System (GIS). The data collection includes global maps from the LRO Wide Angle Camera (WAC, 100 m/px) (Robinson et al., 2010), the Lunar Orbiter Laser Altimeter (LOLA) global Digital Elevation Model (DEM, resolution 118 m/px) (Smith et al., 2017), the Diviner rock abundance (Bandfield et al., 2011) and the Miniature Radio Frequency (Mini-RF) instrument circular polarization ratio (CPR) global maps at ~240 m/px (Cahill et al., 2014), the Clementine UV-VIS color ratio mineral map (e.g., Heather and Dunkin, 2002) as well as the Clementine-derived FeO and TiO_2 maps (e.g., Lucey et al., 2000). Higher resolution panchromatic images and associated Digital Terrain Models (DTMs) from the Kaguya Terrain Camera (TC) onboard the SELENE mission (Haruyama et al., 2008), assembled as mosaics at 7.4 m/px, and LRO

Narrow Angle Camera imagery (NAC, resolutions < 1 m/px) and DTMs (Robinson et al., 2010) were added to the data collection for the four selected landing regions. LRO NAC strips were calibrated and map-projected using the Integrated Software for Imagers and Spectrometers (ISIS) software (Robinson et al., 2010).

3.2 NAC DTM reconstruction

Two existing NAC DTM mosaics (NAC_DTM_ATLAS and NAC_DTM_ATLASVENT) partially cover the Atlas crater floor, at resolutions of 2 and 5 m/px, respectively. Two NAC DTMs were also produced by the LROC team specifically for this project, in the Lacus Somniorum landing area: the NAC_DTM_GROVECRTR01 and NAC_DTM_GROVECRTR02 at 4 and 3 m/px., respectively. These DTMs are publicly available from the LROC data archive (https://www.lroc.asu.edu/archive). To get full topographic data within our final landing ellipses (which were first pre-selected using Kaguya topographic data), additional DTMs at 2 m/px were built from pairs of left and right NAC images (Table 1) using the slope from shading (SfS) technique. SfS exploits the appearance of the shading of an object for 3D reconstruction of its surface or shape. This requires a model of the surface reflectance under variable incidence and emission angles, for which we used the well-known Hapke model (Hapke, 2012). Attempting to reconstruct the 3D shape of an object from one single 2D image results in an ill-posed problem (e.g., Kirk, 1987; Horn, 1990). This difficulty can be alleviated by including information from a DTM of lower resolution than the image itself (e.g., Shao et al., 1991); we used the SLDEM512 (Barker et al., 2016) in this work. The objective function to be minimized by our framework comprises three regularization terms (Grumpe and Wöhler, 2014), corresponding to the integrability error (Horn, 1990) and the deviation of the absolute heights and gradients of a low-pass filtered version of the reconstructed DTM from those of the initial DTM. The DTM construction method does not run on the full image resolution right away but traverses a Laplacian pyramid scheme in order to increase the convergence speed. Each layer of the Laplacian pyramid increases the resolution by a factor of 2. Hence, our algorithm starts at pyramid level 6 (corresponding to $1/2^6 = 1/64$ of the full image resolution). As soon as one level is finished, the next level is initialized by the DTM of the current level interpolated by a factor of 2. This procedure is repeated until a resolution of 2 m/pixel is reached.

Landing area	NAC image pair ID
Mare Frigoris (Atlas crater)	M1369081924
Sinus Iridum	M1099022524
Oceanus Procellarum	M1243998349
Lacus Somniorum	M1108053042

Table 1: List of NAC image pairs (L+ R) used to generate DTMs using the SfS technique.

3.3 Slope analysis

To identify the most suitable location to target for landing (i.e., the center of the landing ellipse) within each candidate area, a statistical slope analysis approach was adopted. It consists of deriving an effective slope map representing the slope at each location as a statistical value (mean and percentiles) of the slopes within an area corresponding to the landing ellipse surrounding this location. A set of ArcGIS tools (slope, focal statistics, zonal statistics, reclassify, editor) were used to this end.

Slopes derived from Kaguya TC DTM mosaics of the four pre-selected areas were used to place candidate ellipses based on the local topography. The “Focal Statistics” tool was used to calculate the mean slope and its standard deviation for a circular area of 4 km radius. The tool thus computes an output raster, for which the value of each output cell represents the mean slope over a 8 km diameter circular area that would be centered on this pixel. In the resulting effective slope map, the candidate ellipse landing locations are selected to be the ones with the lowest mean slope, that is verified to be < 15°. In the final iteration it was verified that 95% of slopes within the candidate ellipse are within this limit. This was done by producing a new raster in which each pixel of slope > 15° was reclassified as a “0” value, whereas each pixel of slope <15° was reclassified as a “1” value before applying zonal statistics.

3.4 Landing ellipse selection and characterization

Statistics (mean, max, min, standard deviation = std) were performed on the generated slope maps, as well as on the Mini-RF CPR and LRO Diviner rock abundance maps in order to determine the presence of centimeter to several-meter-scale objects within the ellipses. Ellipses were then ranked based on both the results of the terrain analysis (slope from Kaguya TC data

at 7.4 m/px and rock abundance) and their scientific interest. For each landing area, one or two final ellipses were selected, and their slope was further analyzed at the NAC scale (2 m/px). In parallel, manual crater and boulder mapping was performed on the individual NAC optical images to check for major obstacles in the landing zone, using all available NAC strips with varying incidence angles (Joulaud et al., this issue). Minor refinements of the ellipse center based on the new slope analysis at 2 m/px and/or on the crater/boulder map were performed when needed, which resulted in subtle differences in lat/long coordinates between the candidate ellipses placed on the Kaguya maps and the final ellipses adjusted with the NAC imagery.

4. Results of the landing ellipse selection

4.1 Southeastern mare Frigoris (including Hercules and Atlas craters)

Located southeast of Mare Frigoris, Atlas (46.7°N, 44.4°E) is a 87 km diameter impact crater in the northeastern quadrant of the nearside of the Moon. Atlas is a well-known floor-fractured crater with a rough and undulated interior that shows concentric and radial fractures, which were interpreted as evidence for post-impact magmatic intrusion at depth (e.g., Schultz, 1976; Losiak et al., 2009; Jozwiak et al., 2012, 2015; Figure 2). Two dark patches that extend over ~ 400 km² (North) and 250 km² (South), respectively, are observed along floor fractures; these patches were previously interpreted as dark mantling deposits, also referred to as pyroclastic deposits (e.g., Gaddis et al., 2003, 2012; Pathak et al., 2021; Flahaut et al., 2023b). The crater's rough topography at a larger scale results from the presence of numerous blocks from a central uplift, as well as slumped, terraced walls (Flahaut et al., 2023b).

Ellipse selection was initially performed in an area covering pyroclastic deposits southeast of Mare Frigoris, in mare deposits within Hercules crater and on the floor of Atlas crater (Figure 2). Rock diversity is, however, much higher in Atlas crater, due to its emplacement within feldspathic highlands and its complex volcanic history (shallow intrusion evidenced by the fractured floor, deeper intrusion evidenced by the central peak composition, eruptions along fractures evidenced by the dark patches; Pathak et al., 2021; Flahaut et al., 2023b, in prep.). In addition to feldspathic material, Atlas crater provides access to pyroclastic deposits, which are a target of interest for both scientific research and future exploration through In Situ Resource Utilization (ISRU) demonstration (e.g., Crawford et al., 2023). The crater floor is also likely to

expose impact rocks. Given the high science value of Atlas crater, which is a geologically diverse, non-mare site, ellipses that fitted the slope criteria in Atlas were ranked the highest (Table 2).

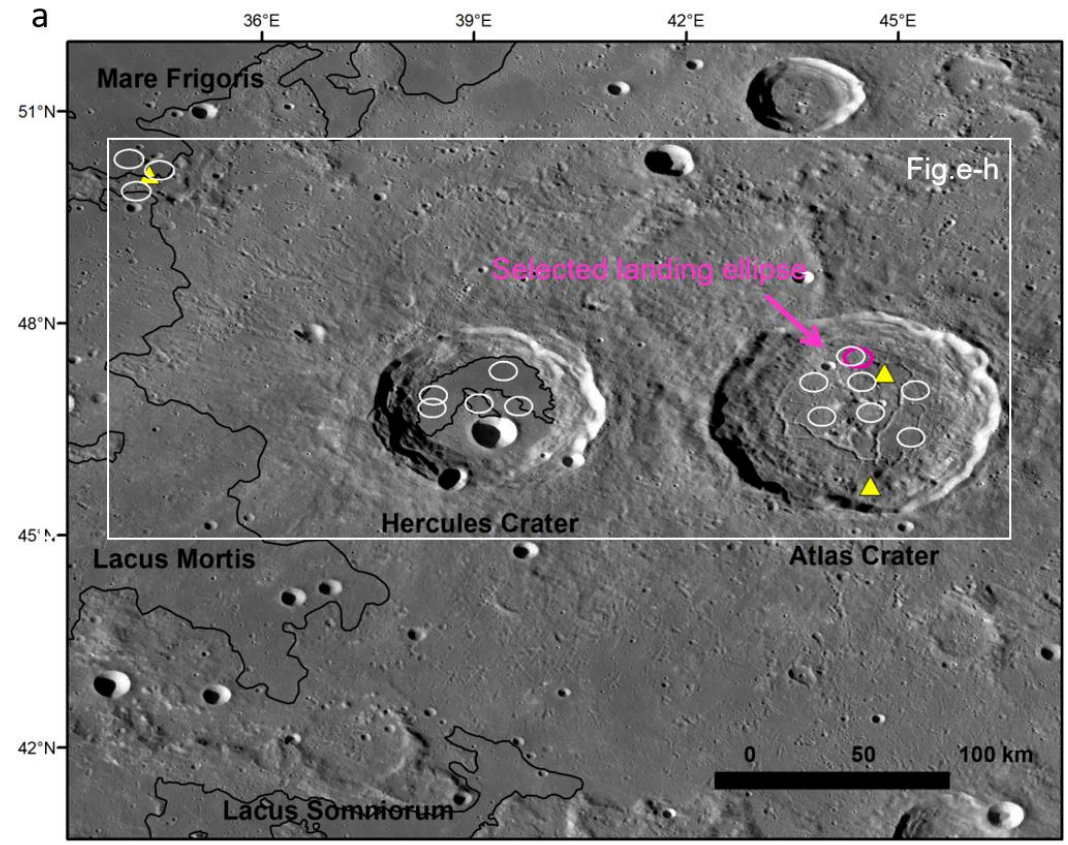

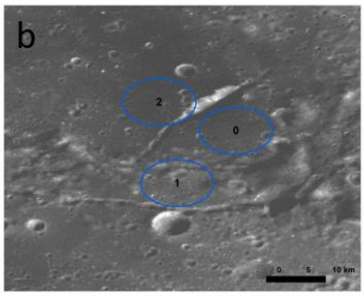

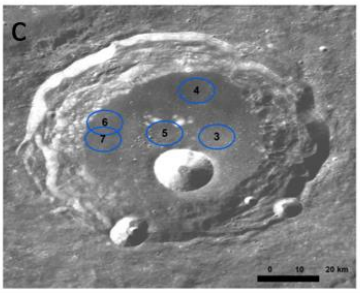

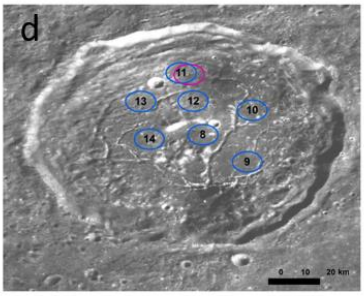

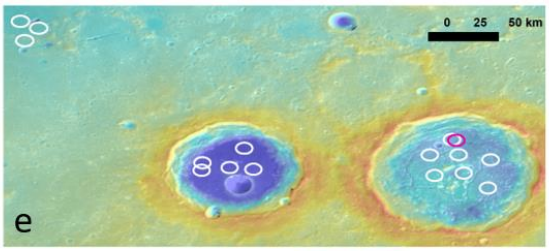

Elevation in m : - 4400 270

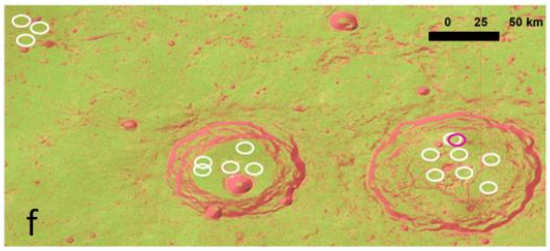

Slope in degrees : 0 15

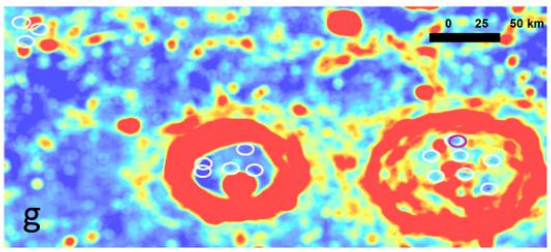

Slope in degrees : 6 10

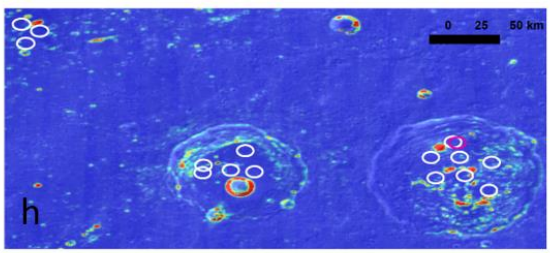

Rock abundance : 0 0,05 %

Figure 2: a) Location of the investigated area (white rectangle) that encompasses southeastern Mare Frigoris (b), Hercules crater (c), and Atlas crater (d). Candidate landing ellipses are displayed in white, whereas the final landing ellipse (Ellipse FR-11) is highlighted in magenta. Yellow triangles represent previously reported pyroclastic deposits from Gaddis et al. (2003). Background = LROC WAC mosaic. b,c,d) Close-ups of Kaguya TC orthoimages; candidate ellipses are displayed in blue and numbered as in Table 2. e) Topography of the investigated area; background = Kaguya TC DTM. f) Slopes within the investigated area, computed from the Kaguya TC DTM. g) Filtered slope map that represents the average mean slopes over an 8 km diameter circle (at the Kaguya TC scale), obtained as a result of the focal statistics tool. h) Rock abundance estimates (expressed as an aerial % of the surface covered by boulders, see Bandfield et al., (2011) for more details) from the Diviner global map. Figures e-h are overlain in transparency over the Kaguya TC orthoimages; all images are shown in a simple cylindrical projection.

Ellipse ID	Location	Center lat (°N)	Center long (°E)	Mean slope at 7.4 m/px (°) (Kaguya TC)	Mean slope standard deviation	Fraction* of pixels with slope <15°	Mean rock abundance (%) (Diviner)	Mean CPR (Mini-RF)
FR-0	Mare Frigoris	50.16	34.55	6.8	4.8	0.94	0.0036	0.59
FR-1	Mare Frigoris	49.87	34.22	6.7	4.4	0.95	0.0034	N/A
FR-2	Mare Frigoris	50.32	34.12	7.3	4.9	0.92	0.0036	N/A
FR-3	Hercules	46.83	39.63	6.2	4.0	0.97	0.0020	0.51
FR-4	Hercules	47.32	39.41	6.3	4.3	0.96	0.0026	N/A
FR-5	Hercules	46.87	39.07	6.9	4.7	0.94	0.0037	N/A
FR-6	Hercules	46.98	38.42	6.0	4.3	0.96	0.0068	N/A
FR-7	Hercules	46.80	38.40	5.5	3.9	0.97	0.0029	N/A
FR-8	Atlas	46.74	44.61	6.8	4.2	0.96	0.0079	0.78
FR-9	Atlas	46.39	45.18	6.9	4.5	0.94	0.0025	N/A
FR-10	Atlas	47.05	45.24	7.3	4.6	0.94	0.0047	0.62
FR-11	Atlas	47.53	44.33	6.8	4.2	0.96	0.0029	0.57
FR-12	Atlas	47.17	44.48	7.0	4.4	0.95	0.0051	0.60
FR-13	Atlas	47.17	43.80	6.9	4.4	0.95	0.0023	0.89
FR-14	Atlas	46.68	43.92	7.1	4.4	0.94	0.0034	0.60

*Table 2: Terrain characteristics of the candidate landing ellipses (initial analysis at the Kaguya TC scale) in the Frigoris area (Hercules and Atlas craters included). *An ellipse in which 100% of the pixels have a slope below 15° would have a value of 1.*

Ellipse FR-11 within Atlas crater was further selected as the prime landing ellipse based on the presence of the northern dark mantling deposit, which extends over the eastern portion of the ellipse, and its terrain characteristics (lower mean slope and rock abundance than ellipse FR-12, which is also straddling over the same pyroclastic deposits). Focal statistics were performed again on the NAC DTM, and the ellipse center was adjusted to account for the difference in slope statistics at the Kaguya TC and NAC scale (Figure 3). The ellipse is generally devoid of fresh impact craters, and dominated by gently rolling plains. Two boulder fields are present on the northern and southeastern edge of the ellipse (Figure 3d).

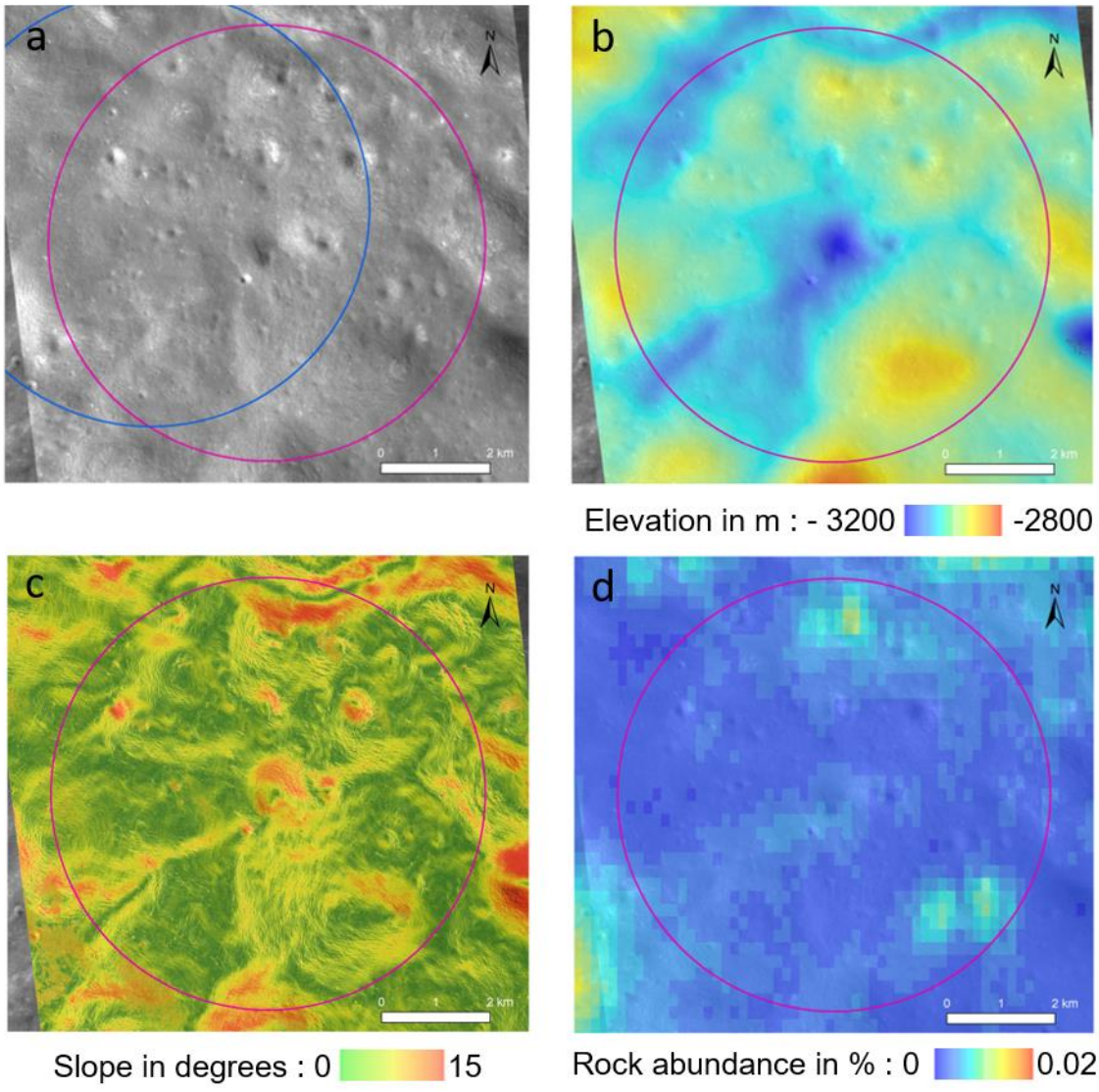

Figure 3: Close-up of the selected landing ellipse (FR-11) in Atlas crater. a) NAC imagery from image pair M1369081924 L + R. The ellipse from the Kaguya TC slope analysis is outlined in blue, whereas the location of the final landing ellipse, after analyses and

refinements at the NAC scale, is outlined in magenta. b) Topography from the SfS-based NAC DTM. c) Derived slope map at the NAC scale (2 m/pixel). d) Close-up of the Diviner rock abundance estimates within the final landing ellipse. Data are projected in a custom orthographic projection using the final landing ellipse center coordinates (47.5117° N; 44.4294° E) as the reference latitude and longitude.

4.2 Sinus Iridum

Centered around 44.1° N, 31.5° W, the 249 km diameter Sinus Iridum basin is a semi-enclosed crater superimposed on the northern rim of the Imbrium Basin (Figure 4a). Previous studies demonstrated that the basin is filled by several mare units with thicknesses up to 500 m (Thomson et al., 2009; Staid et al., 2011; Thiessen et al., 2014) and ages ranging from ~ 3.37 Ga to 1.24 Ga, with a general decrease in age from the northeast to the southwest (Hu et al., 2020). A number of volcanic and tectonic features such as vents, sinuous rilles, and wrinkle ridges have been observed in the area (e.g., Qiao et al., 2014; Wu et al., 2018), together with secondary impact crater chains from nearby Copernican craters (e.g., Schaber, 1969).

While our early investigations considered the full basin, final candidate landing ellipses were searched for along the northern rim of the basin, where the geological diversity is highest. Four candidate ellipses were placed in proximity to the highlands and at the putative location of a 20 km × 70 km intrusive volcanic complex, as suggested by numerous rilles and possible vents (Figure 4b, c) as well as in areas of low average slope according to the Kaguya TC DTM (Figure 4e). Statistics of all four candidate ellipses are reported in Table 3.

Ellipse ID	Center lat (°N)	Center long (°E)	Mean slope at 7.4 m/px (°) (Kaguya TC)	Mean slope standard deviation	Fraction of pixels with slope <15°	Mean rock abundance (%) (Diviner)	Mean CPR (Mini-RF)
SI-0	47.21	-29.46	7.0	4.6	0.94	0.0029	N/A
SI-1	46.94	-27.37	6.6	4.4	0.95	0.0047	N/A
SI-2	47.09	-28.36	7.0	4.6	0.94	0.0031	N/A
SI-3	47.25	-29.10	7.0	4.6	0.94	0.0037	0.57

Table 3: Terrain characteristics of the candidate landing ellipses (initial analysis at the Kaguya TC scale) in the Sinus Iridum area.

Ellipse SI-1 was further selected based on its terrain characteristics (low mean slope and rock abundance), but also based on its proximity to a kipuka (i.e., a portion of highland surrounded by more recent lava flows) to the northeast and a possible vent to the southeast. A probable

rille also crosses the northwestern quadrant of the ellipse, and several crater chains are visible. Focal statistics were again performed on the NAC DTM, and the ellipse center was adjusted to account for the difference in slope statistics at the Kaguya TC and NAC scale (Figure 5a). Whereas the elevation does not vary much within the final ellipse, several small sharp craters (including secondaries) and boulder fields are present within the western part of the ellipse (Figure 5).

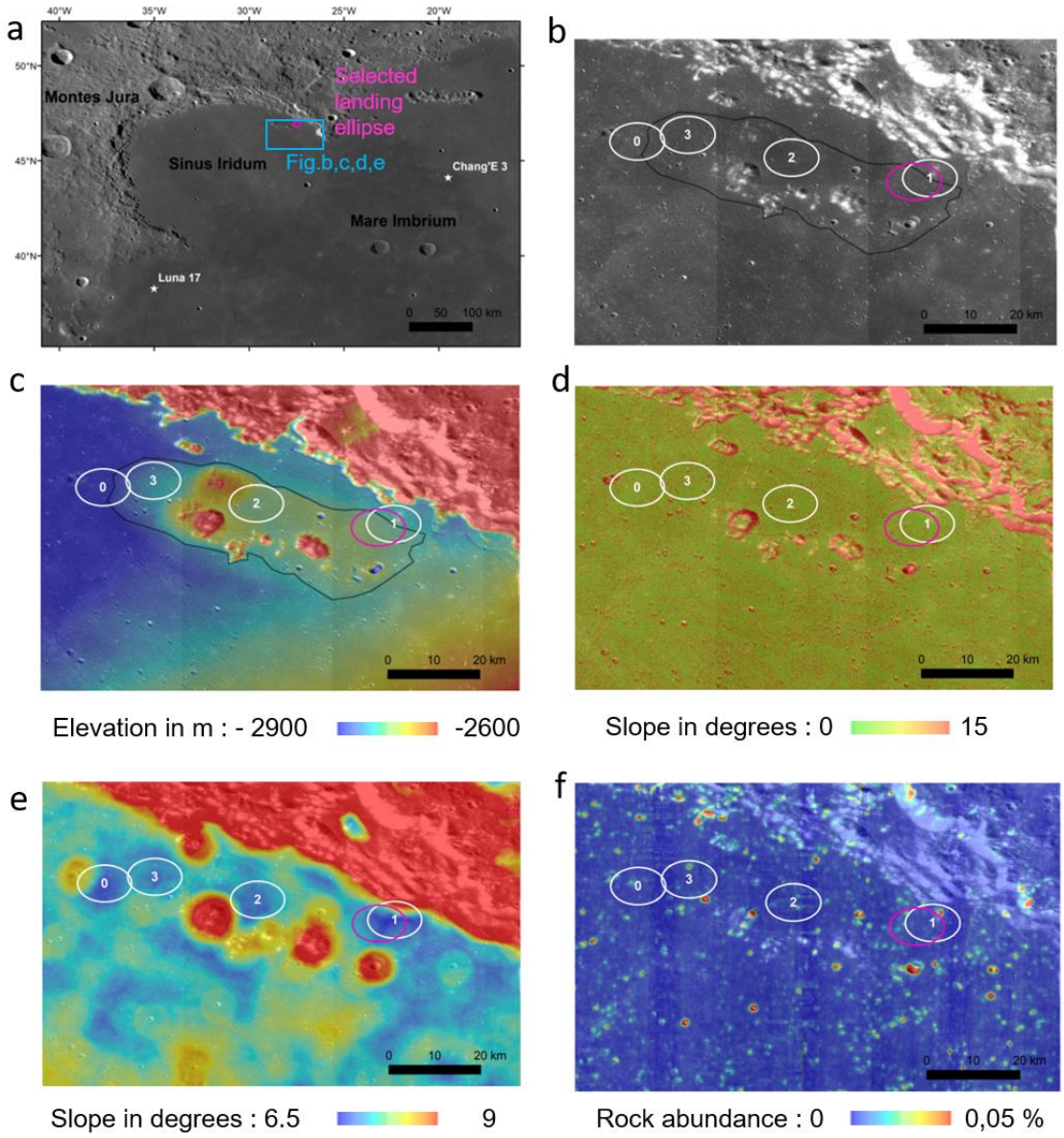

Figure 4: a) Location of Sinus Iridum, the investigated area (blue rectangle), and the final landing ellipse (Ellipse SI-1, in magenta); background = LROC WAC mosaic. b) Close-up of a putative intrusive volcanic complex near the northern rim (black outline), targeted for the ellipse search; background = Kaguya TC orthoimages. Candidate ellipses from the Kaguya

slope analysis are represented in white, whereas the final landing ellipse (ellipse SI-1, which was repositioned after analysis at the NAC scale) is displayed in magenta. c) Topography of the investigated area; background = Kaguya TC DTM. d) Slopes within the investigated area, computed from the Kaguya TC DTM. e) Filtered slope map that represents the average mean slopes over a 8 km diameter circle (at the Kaguya TC scale), obtained as a result of the focal statistics tool. f) Rock abundance estimates from the Diviner global map. Figures c to f are overlain in transparency over the Kaguya TC orthoimages; all images are shown in a simple cylindrical projection.

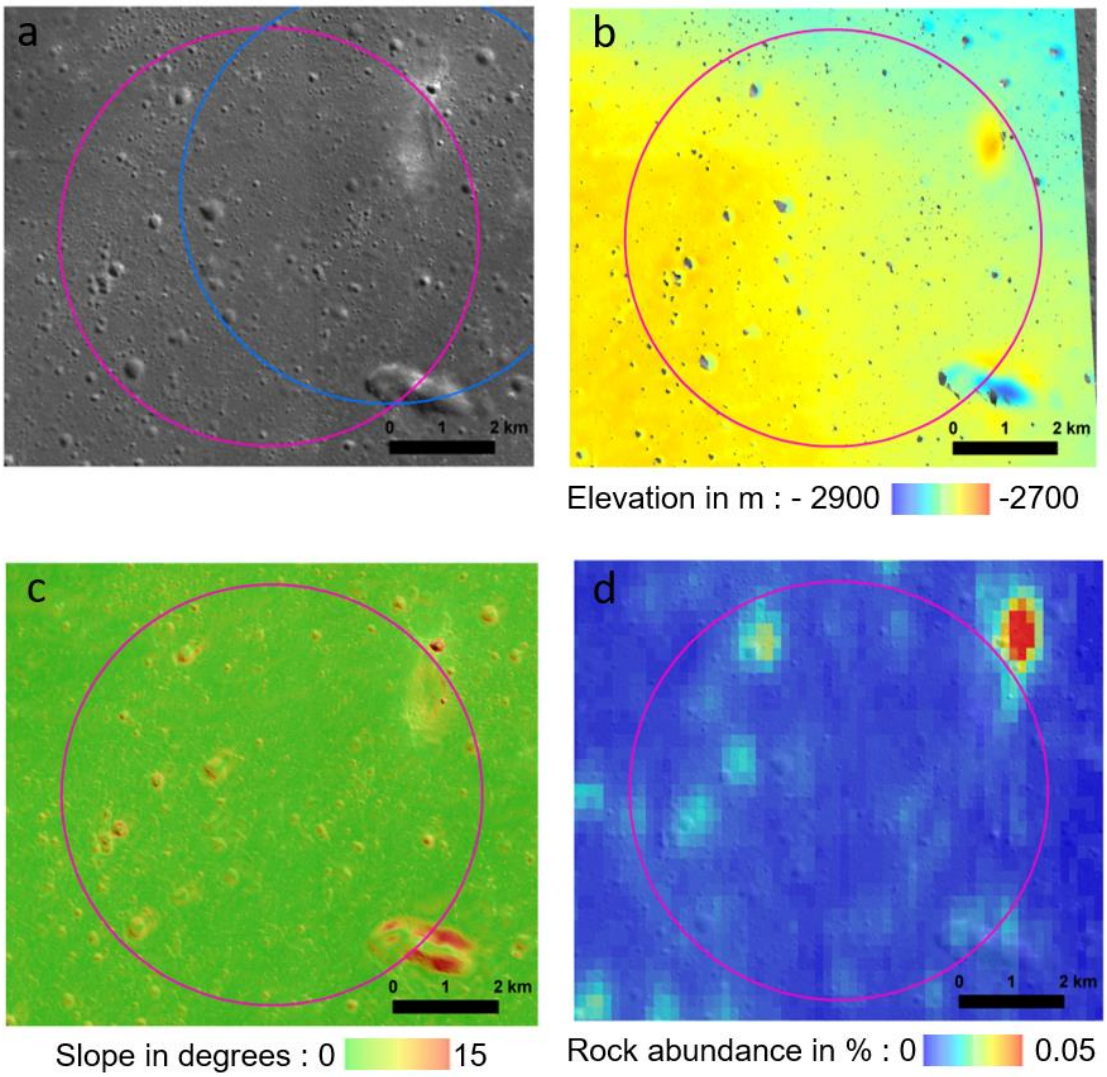

Figure 5: Close-up of the selected landing ellipse (SI-1) in Sinus Iridum. a) NAC imagery from image pair M1099022524 L + R. The ellipse from the Kaguya TC slope analysis is outlined in blue, whereas the location of the final landing ellipse, after analyses and refinements at the NAC scale, is outlined in magenta. b) Topography from the SfS-based NAC DTM. c) Derived

slope map at the NAC scale (2 m/px). d) Close-up of the Diviner rock abundance estimates within the final landing ellipse. Data are projected in a custom orthographic projection using the final landing ellipse center coordinates (46,9180° N; 27,4860° W) as the reference latitude and longitude.

4.3 Oceanus Procellarum

Located on the western nearside of the Moon, Oceanus Procellarum is the largest lunar mare (~ 1.7×10^6 km^2). Specificities of this irregular, elongated mare unit include the presence of the youngest known mare basalts (~1.3 Ga, estimated from crater counts) toward its center (Hiesinger et al., 2003) and the presence of numerous large volcanic complexes, such as Marius Hills and Mons Rümker (e.g., Whitford-Stark and Head, 1980; Figure 6a).

Our study area is located between 39.5-44.5°N and 45-53°W, in an area previously investigated as a possible landing site for the Chang'E-5 mission (Qian et al., 2018), and in proximity to the Mairan domes (Figure 6a, b). The four volcanic domes exhibit low values on the Diviner Christiansen Feature map, which was previously interpreted as evidence for high silica abundances (Glotch et al., 2011). Candidate ellipses were placed in the flattest areas along the Rima Sharp sinuous rille (PR-7), close to the boundary with the highlands (PR-0, PR-2, PR-5, PR-6), and in proximity of the Mairan domes (PR-1, PR-2, PR-3, PR-4) (Figure 6). The latter were ranked more highly, due to the high science value of these previously unvisited, silicic outcrops (Table 4). Among the four domes, ellipse PR-4 in proximity to the cone-shaped Mairan-T volcano was preferred due to its low slope and rock abundance, but also its proximity to this unique edifice with a well-preserved summit crater.

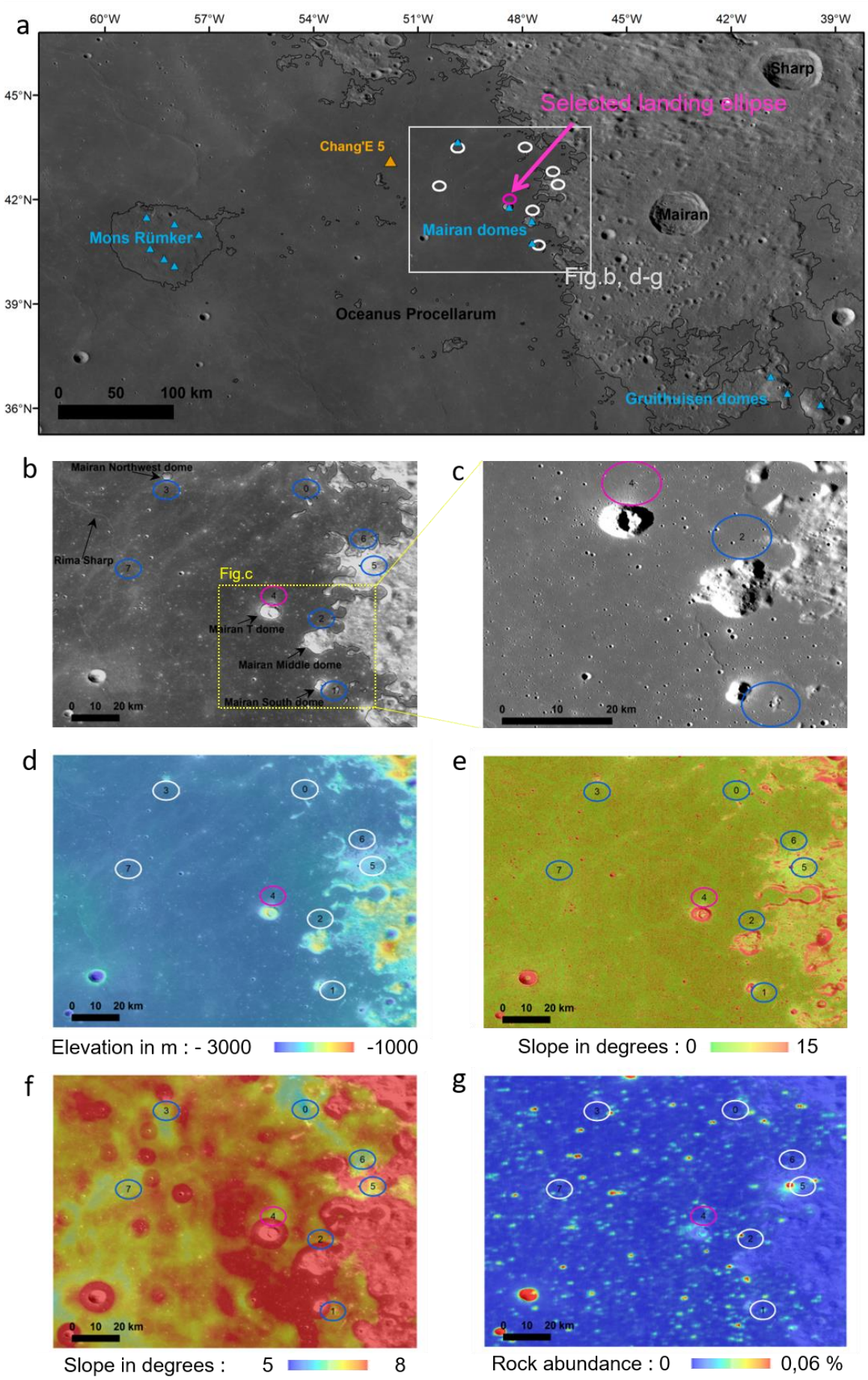
a
60°W
57°W
54°W
51°W
48°W
45°W
42°W
39°W
45°N
42°N
39°N
36°N
Sharp
Selected landing ellipse
Chang'E 5
Mairan
Mairan domes
Mons Rümker
Fig.b, d-g
Oceanus Procellarum
0 50 100 km
Gruithuisen domes
b
Mairan Northwest dome
Rima Sharp
Fig.c
Mairan T dome
Mairan Middle dome
Mairan South dome
0 10 20 km
c
0 10 20 km
d
0 10 20 km
Elevation in m : - 3000
-1000
e
0 10 20 km
Slope in degrees : 0
15
f
0 10 20 km
Slope in degrees :
5
8
g
0 10 20 km
Rock abundance : 0
0,06 %

Figure 6: a) Location of the investigated area (white rectangle) within Oceanus Procellarum. Candidate landing ellipses are displayed in white, whereas the final landing ellipse (Ellipse PR-4) is highlighted in magenta. Blue triangles represent previously reported volcanic domes from Glotch et al., (2011) and Lena al. (2013), whereas the orange triangle represents the landing site of the Chang'E-5 mission; background = LROC WAC mosaic. b,c) Close-ups of Kaguya TC orthoimages, candidates ellipses are displayed in blue and numbered as in Table 4. d) Topography of the investigated area from the Kaguya TC DTM. e) Slopes within the investigated area, derived from the Kaguya TC DTM. f) Filtered slope map that represents the average mean slopes over an 8 km diameter circle (at the Kaguya TC scale), obtained as a result of the focal statistics tool. g) Rock abundance estimates from the Diviner global map. Figures d to f are overlain in transparency over the Kaguya TC orthoimages; all images are shown in a simple cylindrical projection.

Ellipse ID	Center lat (°N)	Center long (°E)	Mean slope at 7.4 m/px (°) (Kaguya TC)	Mean slope standard deviation	Fraction of pixels with slope <15°	Mean rock abundance (%) (Diviner)	Mean CPR (Mini-RF)
PR-0	43.50	-47.92	6.2	4.4	0.96	0.0051	N/A
PR-1	40.69	-47.54	7.5	5.0	0.92	0.0049	N/A
PR-2	41.69	-47.71	7.3	4.9	0.93	0.0071	N/A
PR-3	43.49	-49.86	6.8	4.7	0.94	0.0054	0.45
PR-4	42.01	-48.37	6.9	4.6	0.94	0.0064	N/A
PR-5	42.43	-46.98	7.2	5.2	0.93	0.0132	N/A
PR-6	42.81	-47.12	6.5	4.4	0.95	0.0045	N/A
PR-7	42.39	-50.39	6.8	4.6	0.94	0.0057	N/A

Table 4: Terrain characteristics of the candidate landing ellipses (initial analysis at the Kaguya TC scale) in the Oceanus Procellarum area.

The mare area in Oceanus Procellarum is relatively flat, and no refinements were needed at the NAC DTM scale. The ellipse was placed as close as possible to the northern edge of the Mairan T dome, but far enough to avoid its steep slopes (Figure 7b). Similarly to Sinus Iridum, the final ellipse in Oceanus Procellarum presents several sharp, small impact craters and boulder fields, mostly along its northern and southern edges (Figure 7; Joulaud et al., this issue).

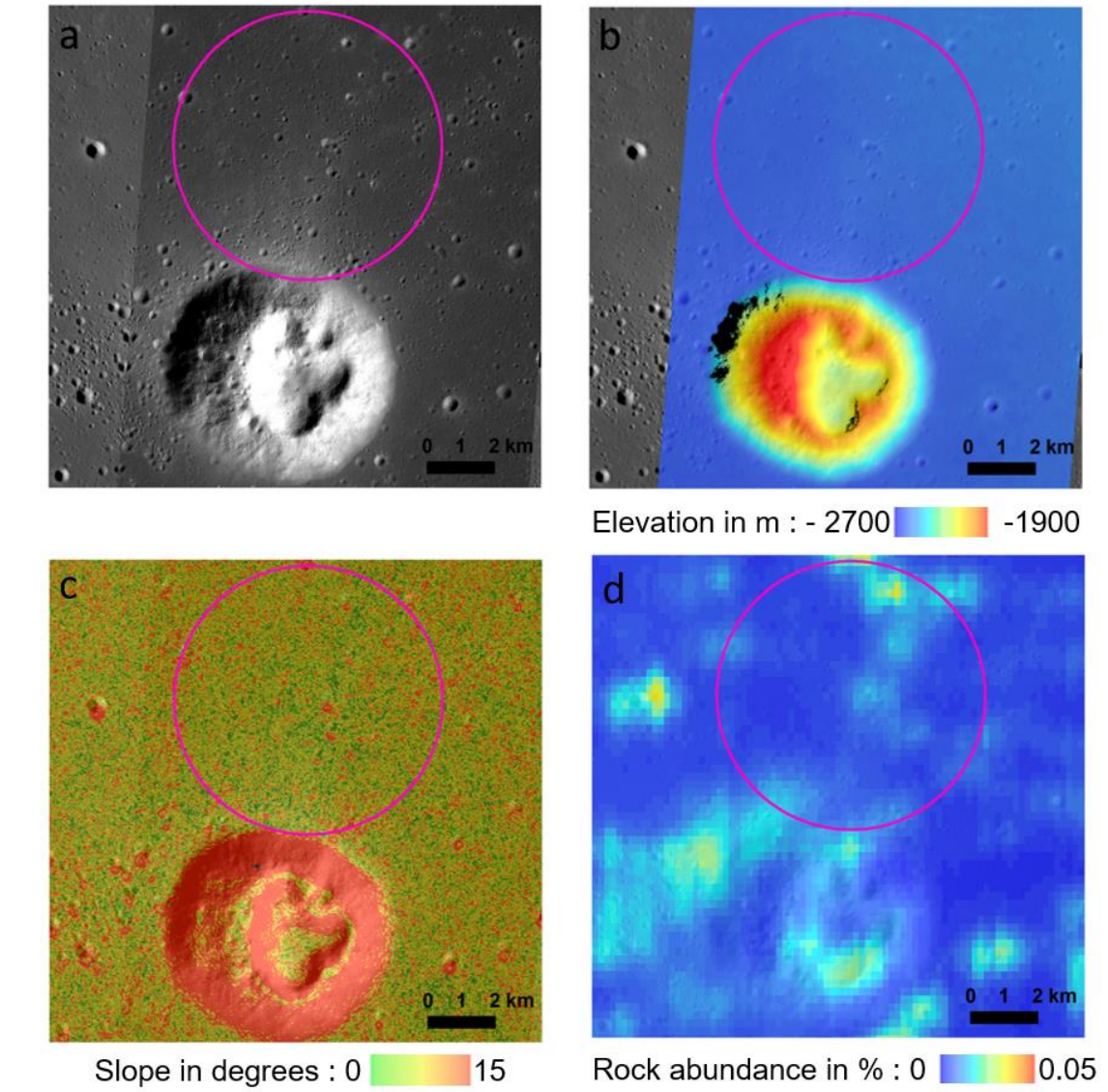

Figure 7: Close-up of the selected landing ellipse (PR-4) in Oceanus Procellarum. a) NAC imagery from image pair M1243998349 L + R. The location of the final landing ellipse is outlined in magenta. b) Topography from the SfS-based NAC DTM. c) Derived slope map at the NAC scale (2 m/px). d) Close-up of the Diviner rock abundance estimates within the final landing ellipse. Data are projected in a custom orthographic projection using the final landing ellipse center coordinates (42.0134° N; 48.3700° W) as the reference latitude and longitude.

4.4 Lacus Somniorum

Located between 31-42° N, 20-42° E on the nearside of the Moon, Lacus Somniorum is a vast volcanic plain with irregular and poorly defined boundaries. Little is known about this feature stretching north of Mare Serenitatis (Figure 8a). Ellipse selection was performed on a 30 km

by 40 km area located southeast of the 28 km diameter Grove Crater, straddling various geological units according to the geologic map of Scott (1972), Grolier (1974), and Fortezzo et al. (2020): the Imbrian Alpes formation of feldspathic nature (Ia), Imbrian plains of unknown nature (Ip), mare basalts (Im), and the ejecta of Grove crater (Itd) (Figure 8b).

As Lacus Somniorum was initially pre-selected as the prime landing site for the ELM in 2020, Flahaut et al. (2021) had already performed a detailed slope analysis searching for a 4 km diameter landing ellipse. Four candidate ellipses were proposed (Figure 4c-e), and manual mapping of craters and boulders was performed (Breton et al., 2021). Crater counts suggested an age of 3.71 ± 0.06 Gy for the mare basalt units, which were targeted by the prime landing ellipse (Flahaut et al., 2021). Analyses of Clementine data revealed relatively low FeO (~12 wt%) and TiO_2 (~0.9 wt%) concentrations in the targeted Im unit, suggesting the mare may consist of unusual, Al-rich basalts (Flahaut et al., 2021). Despite modifications in the landing ellipse size (8 km diameter instead of 4 km) and landing site priorities, we kept the primary landing ellipse (LS-3) initially selected by the ELM team but extended its size to meet the new constraints. Statistics obtained for the 8 km diameter ellipse centered at 38,92° N and 33,82° E are presented in Table 5, whereas a close-up of high-resolution imagery is shown in Figure 9. The final ellipse shows a gradual decrease in elevation from the southeast to the northwest, with evidence for few boulders only from orbit (Figure 9; Joulaud et al., this issue).

Ellipse ID	Center lat (°N)	Center long (°E)	Mean slope at 7.4 m/px (°) (Kaguya TC)	Mean slope standard deviation	Fraction of pixels with slope <15°	Mean rock abundance (%) (Diviner)	Mean CPR (Mini-RF)
LS-3	38.92	33.82	7.5	4.9	0.95	0.0021	0.52

Table 5: Terrain characteristics of the final landing ellipse in Lacus Somniorum, at the Kaguya TC scale.

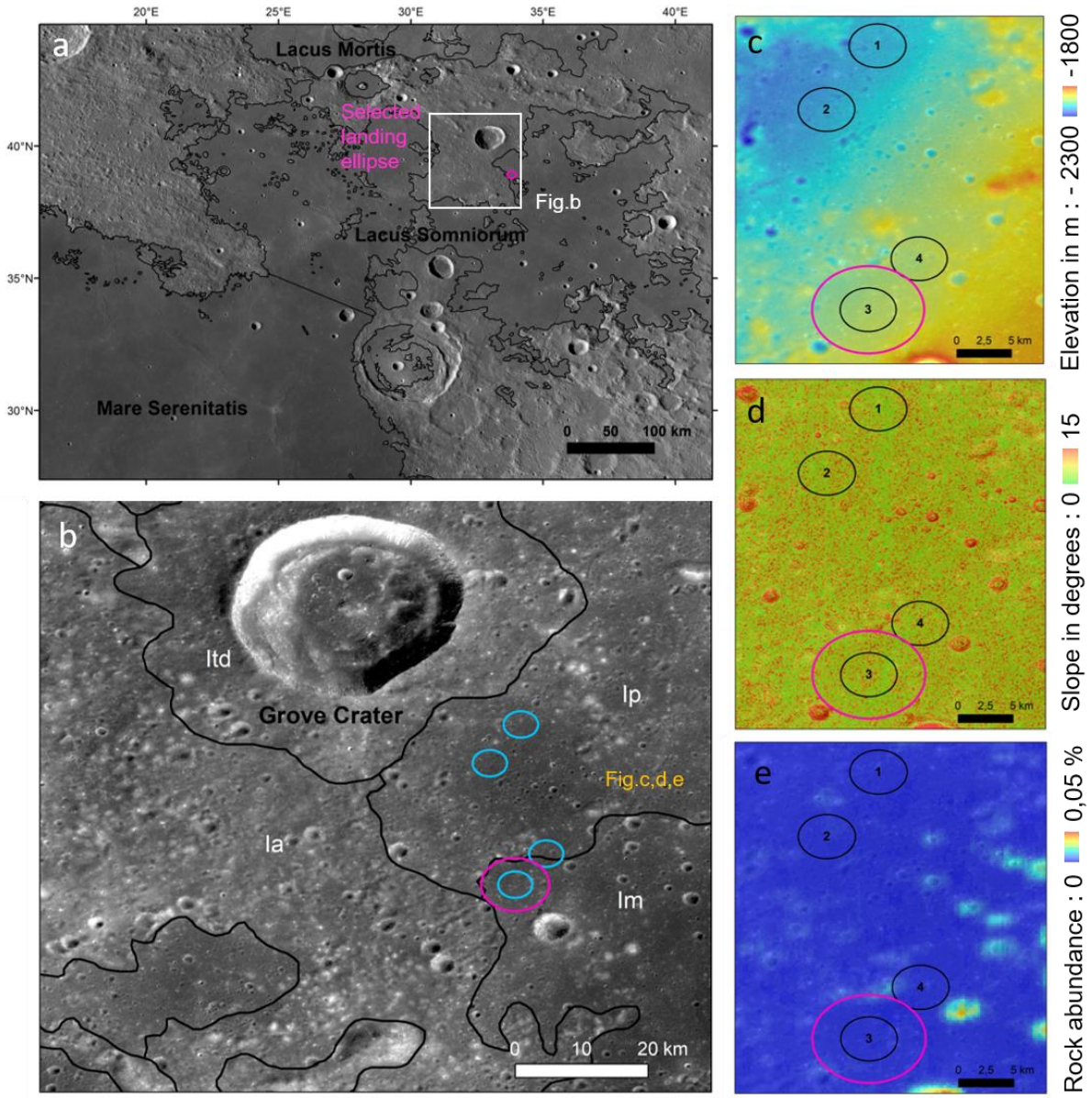

Figure 8: a) Location of Lacus Somniorum, the investigated area southeast of Grove crater (white rectangle), and the final landing ellipse (Ellipse LS-3, in magenta); background = LROC WAC mosaic. b) Close-up of the investigated area for the ellipse search; background = Kaguya TC orthoimages. Four-kilometer diameter candidate ellipses from the initial Kaguya slope analysis of Flahaut et al. (2021) are represented in blue, whereas the final 8 km diameter landing ellipse (ellipse LS-3) is displayed in magenta. c) Topography of the investigated area; background = Kaguya TC DTM. d) Slopes within the investigated area, computed from the Kaguya TC DTM. e) Rock abundance from the Diviner global map. Figures c to e are overlain in transparency over the Kaguya TC orthoimages; all images are shown in a simple cylindrical projection.

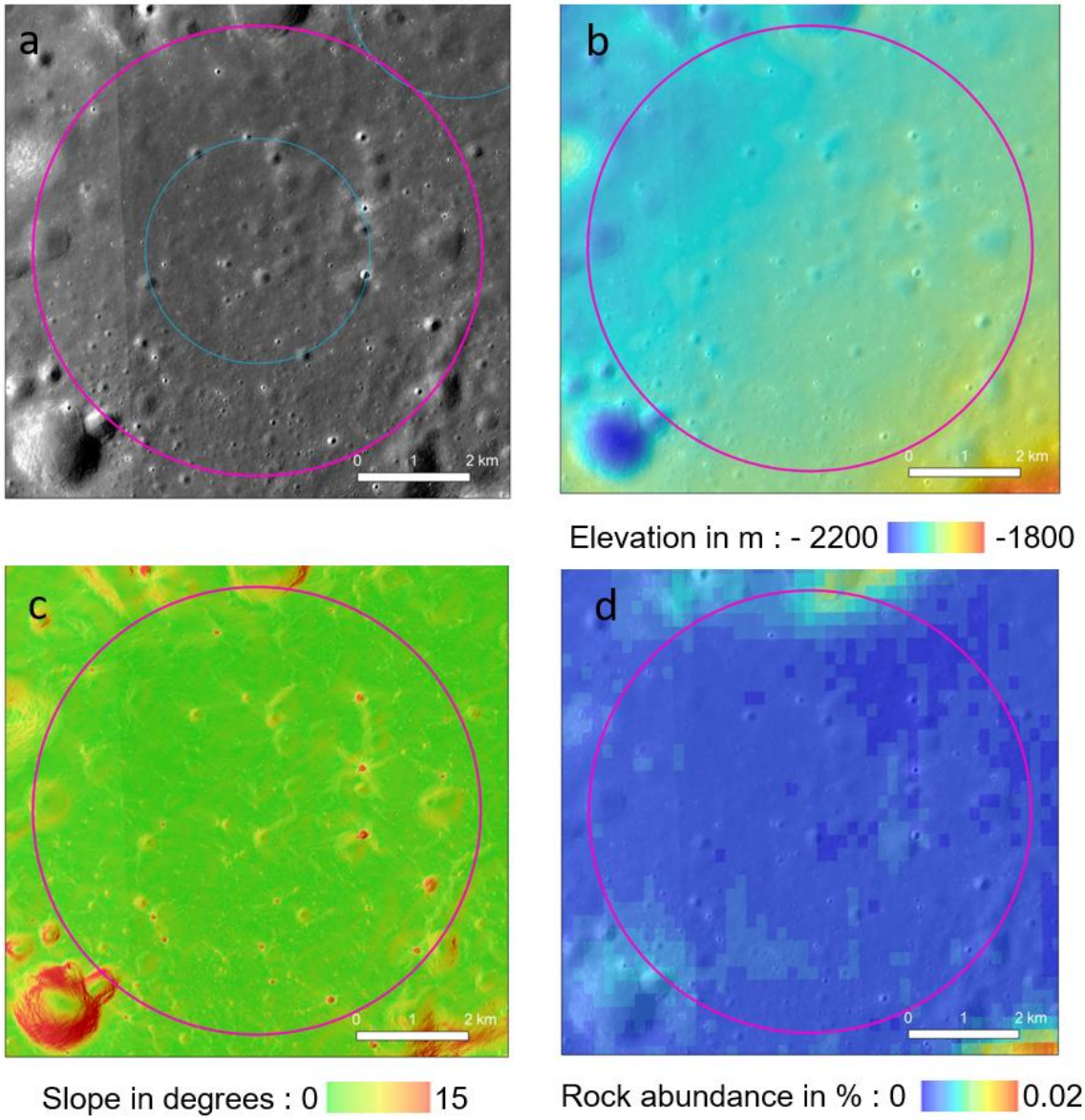

Figure 9: Close-up of the selected landing ellipse (LS-3) in Lacus Somniorum. a) NAC imagery from image pair M1108053042 L + R. The previous 4 km diameter landing ellipse from Flahaut et al. (2021) is outlined in blue, whereas the location of the final 8 km diameter landing ellipse is outlined in magenta. b) Topography from the SfS-based NAC DTM. c) Derived slope map at the NAC scale (2m/pixel). d) Close-up of the Diviner rock abundance estimates within the final landing ellipse. Data are projected in a custom orthographic projection using the final landing ellipse center coordinates (38,9200°N; 33,8150°E) as the reference latitude and longitude.

5 Discussion

5.1 Comparison of the candidate landing sites

A summary of the four candidate landing site characteristics is presented in Table 6. All selected ellipses are relatively flat, with mean slopes between 6.7 and 8.0° at the Kaguya TC scale, and between 1.9 and 4.8° at the NAC scale. This difference in mean slope is not only due to the difference in resolution between the DTMs derived from Kaguya TC data and LRO NAC data, respectively, but mainly to the presence of noise artifacts in the 3D data contained in the Kaguya TC stereo DTM (see Section 5.2). Lower Diviner average rock abundance values are observed for Lacus Somniorum and Atlas crater, as confirmed by the visual analyses of NAC images, which reveal the presence of few boulders (see Joulaud et al., this issue). In contrast, Sinus Iridum and Oceanus Procellarum show higher average rock abundances than the average of 0.004 % obtained for the lunar surface at latitudes of ±60° (Bandfield et al., 2011). Both of these sites are located in relatively young mare units (i.e., younger than those previously visited by the Apollo missions) and are also marked by the presence of numerous sharp, secondary craters.

All four sites are technically attainable by a lunar lander such as Hakuto-R and offer different and diverse science targets. While ellipses in Sinus Iridum and Lacus Somniorum are located upon mare units but in proximity to highland material, the selected ellipse in Oceanus Procellarum is located north of the Mairan T silicic dome. The selected ellipse in Atlas is straddling a part of the crater floor that is of feldspathic nature to the west and a pyroclastic deposit to the east.

Site	Order in landing sequence	Age (Gy)	Kaguya TC mean slope (°) at 7.4 m/px for 8 km ellipse	NAC mean slope (°) at 2 m/px for 8 km ellipse	Diviner mean rock abundance (%)	Features of interest
Atlas crater	1	3.8	8.0	4.8	0.0028	Floor-fractured crater with a complex volcanic history including pyroclastics, highland floor

Sinus Iridum	2	3.4	6.7	2.0	0.0045	Proximity to highlands/kipukas, possible intrusive plateau
Oceanus Procellarum	3	1.3	6.9	2.8	0.0064	Silicic dome (Mairan T dome), young mare
Lacus Somniorum	4	3.7	7.5	1.9	0.0021	Proximity to highlands/kipukas, mare of unusual composition

Table 6: Summary of the characteristics of the four candidate landing sites.

5.2 Slope error assessment

Due to the difference in baseline between the Kaguya-based DTM and NAC-based DTM, mean slope values vary by up to ~ 6° (Table 6). In addition, small inaccuracies in the matching procedure between stereo images resulted in noise in the Kaguya DTM, which led to higher derived slope values. Most stereo algorithms preferentially extract disparities between the stereo images that are close to integer values, an effect called pixel-locking (Gehrig and Franke, 2016). As a result, the Kaguya DTMs exhibit a high frequency, "crumpled" structure in areas that are actually even, so that small details on spatial scales close to the resolution limit are unreliable and may in many cases be artifacts.

The SfS-generated LROC NAC DTM of this study also differ from the standard stereo-derived NAC DTM provided by the PDS, bearing some uncertainties in the slope assessment. In turn, the SfS method strongly depends on the validity of the employed reflectance model. The Hapke model (Hapke, 2012) used in this work for SfS analysis is known to provide an accurate description of the reflectance of planetary regolith surfaces in general. However, albedo variations on spatial scales much smaller than the resolution of the low-resolution reference DTM, such as ejecta blankets of small fresh craters, might produce artifacts in the SfS-derived DTM.

Such errors may lead to erroneous (and often overestimated) slope values for a limited number of pixels. We note, however, that the calculated mean slopes within our selected ellipses, at

both the Kaguya and NAC scales, are well below the threshold of 15° and thus did not require the application of a safety margin.

5.3 Cross-investigations with the ELM Rashid-1 rover

Carrying two panoramic imagers, a microscopic and a thermal camera, four Langmuir probes, and a material adhesion experiment (MAD), the Rashid-1 rover was designed to investigate regolith properties and plasma environment at the surface of the Moon (Almarzooqi and AlMaeeni, 2021; Els et al. 2021; Els et al., this issue). With a pixel size of ~25 microns (Els et al., this issue), the microscopic imager CAM-M would have been able to resolve most individual grains of the regolith; notably, at the Apollo landing sites, typical mean diameters of regolith particles vary between 45 and 100 µm, with an average mean diameter of ~80 µm (e.g., Carrier 1973; McKay et al. 1991; Lucey et al. 2006). With a field of view of 82° and a resolution of 0.04°/px, the panoramic imagers CAM-1 and 2 would have offered the possibility to investigate rocks, boulders, and possible vertical sections (ridges, crater walls) at high resolution, providing clues on the vertical organization and thickness of the regolith (Virmontois et al., in prep.). Lateral variations within the regolith could have been surveyed along the rover traverse, whereas mechanical properties of the regolith could have been derived from the rover tracks (e.g., Mitchell et al., 1972; Tang et al., 2020; Basilevsky et al., 2021) and the MAD experiment (Els et al., this issue).

In addition to these general scientific investigations and to possible cross-correlation / ground -truthing for remote sensing observations, specific targets could have been surveyed at each of the four candidate landing sites. The prime landing site Atlas crater provided, for the first time, access to the floor of a complex impact crater that is presumably of feldspathic composition (with possible impact melt and breccias). Regolith properties in Atlas may be different from sites investigated by previous missions, as suggested by its unique “elephant hide” texture (Joulaud et al., this issue). NAC imagery indeed reveals gently rolling plains with small-scale ridges, largely devoid of craters (Figure 3; Flahaut et al., 2023b). The eastern part of the ellipse encompasses darker materials mapped as pyroclastic deposits. Although the Rashid-1 rover was not equipped with any instrument to measure rock or regolith compositions, it could have investigated the proportion of glass/quenched materials in pyroclastic deposits from images and, thus, provided constraints on the grain sizes, texture and opacity of pyroclastic deposits. In addition to monitoring temperature variations, the CAM-T thermal imager could have been

used to survey the thermal inertia properties of the various highland, impact-derived, and volcanic material in Atlas. Understanding the properties of regolith and pyroclastic deposits, and their lateral variations, especially at a non-mare site such as Atlas crater is a key objective for scientists but also for future ISRU demonstrations (e.g., Crawford et al., 2023; Flahaut et al., 2023a), as only few highland locations have been investigated by the Apollo and Luna missions.

Investigations in Sinus Iridum, Oceanus Procellarum or Lacus Somniorum would have primarily focused on mare material. In Sinus Iridum, the occurrence of kipukas and craters with large boulders suggests that rocks from the nearby highlands would have been accessible at selected location (Figure 5). Oceanus Procellarum would have offered access to a relatively young (~1.3 Gy; Hiesinger et al., 2003) mare regolith, which appears to contain more rocks and boulders than the other sites (Joulaud et al., this issue). The presence of the Mairan T silicic dome at the southern end of the ellipse (Figure 7) suggests that rocks of evolved composition, possibly akin to the granitic clasts observed in several Apollo breccias (e.g., Rutherford et al., 1976; Seddio et al., 2013 and references therein), could have been encountered. Although similar to most mare basalts in terms of age (Hiesinger et al., 2000,2011; Flahaut et al., 2021), the Lacus Somniorum candidate site would have provided access to an unvisited and poorly studied region of unusual composition (Flahaut et al., 2021). Indeed, low Fe and Mg abundances were reported for this mare region and tentatively interpreted as evidence for the presence of high-Al basalts or mixed highland and mare regolith (e.g., Flahaut et al., 2021; Kramer et al., 2015); the latter hypothesis could have been tested in situ by the Rashid-1 rover.

6 Conclusions

The procedure for selecting the four landing sites of the Emirates Lunar Mission Rashid-1 mission, namely Atlas crater (prime), Sinus Iridum, Oceanus Procellarum, and Lacus Somniorum (back-ups) was presented. High resolution remote sensing imagery and topography data were used to place candidate ellipses within these four regions, which were then ranked quantitively based on the terrain characteristics (slope and rock abundance) and qualitatively based on their scientific merit. This approach allowed us to maximize possible science outcomes by prioritizing targets of high scientific value rather that prime terrain conditions, as long as the proposed locations met the engineering requirements. Features of interest were identified at the various sites, including kipukas, silicic domes, unusual mare compositions and

volcanic products. The prime landing site Atlas crater would have provided, for the first time, access to the floor of a complex impact crater of feldspathic composition. Along the rover traverse, investigations of rock diversity, regolith properties, geological structures and plasma parameters were foreseen, with records of spatial and / or temporal variations. With a small payload but optimized landing site selection, the Rashid-1 rover could have shed light on numerous hot topics in lunar science such as the origin of non-mare volcanism or the evolution of regolith properties and stratigraphy (e.g., Flahaut et al., 2012, 2023a). Despite the unfortunate fate of the mission, all four sites therefore remain valuable targets for future lunar missions, with numerous key science questions to be addressed at these locations.

7 Acknowledgments

This work is part of the framework of the Emirates Lunar Mission (ELM). The ELM is conducted by the Mohammed Bin Rashid Space Center (MBRSC), in Dubai, UAE. The ELM is funded by the ICT Fund as part of the Mars 2117 initiative. Support from the French space agency (CNES) to J.F., M.J., S.B., and E.F. is much appreciated. The authors wish to express their gratitude to the LROC team (and especially Mark Robinson and Madeleine Manheim) for the availability of the data, and their support in imaging the ELM candidate sites throughout the entire landing site selection process. Feedback from the ispace company during the selection process was much appreciated. The authors are also grateful for helpful comments from guest editor Maryam Yousuf, Joshua Cahill, Sebastien Besse and an anonymous reviewer. Finally, the authors are grateful to the ELM and CNES FOCSE teams for such an amazing opportunity and experience, and to co-workers and interns at CRPG who have supported various stages of the project development. This is CRPG contribution n°2853.

Data availability statement

Diviner, Mini-RF and LRO WAC global mosaics were downloaded from the NASA Planetary Data System (https://pds-geosciences.wustl.edu/dataserv/moon.html). LROC NAC images and the LROC team DTMs are available from the LROC data node (http://lroc.sese.asu.edu/). Kaguya TC images and DTMs are also publicly available on the JAXA's SELENE Archive (https://darts.isas.jaxa.jp/planet/pdap/selene/). NAC DTMs that were generated in this study

can be downloaded from the OTELo Research Data Repository (ORDAR) at http://dx.doi.org/10.24396/ORDAR-125.

Competing Interests

The authors have no competing interests to declare that are relevant to the content of this article.

7 References

Almarzooqi, H., & S. AlMaeeni (2021). Rashid Rover: A Small Rover with Big Science Goals, IAC-15-E4.2.8, 72nd International Astronautical Congress (IAC), Dubai, United Arab Emirates, 25-29 October 2021.

Bandfield, J. L., R.R. Ghent, A.R. Vasavada, D.A. Paige, S.J. Lawrence & M.S. Robinson (2011). Lunar surface rock abundance and regolith fines temperatures derived from LRO Diviner Radiometer data. Journal of Geophysical Research: Planets, 116(E12).

Barker, M. K., Mazarico, E., Neumann, G. A., Zuber, M. T., Haruyama, J., Smith, D. E. (2016). A new lunar digital elevation model from the Lunar Orbiter Laser Altimeter and SELENE Terrain Camera. Icarus 273, 346-355.

Basilevsky, A. T., Malenkov, M. I., Volov, V. A., Abdrakhimov, A. M., Kozlova, N. A., Zubarev, A. E., & Nadezhdina, I. E. (2021). Estimation of the Strength of the Lunar Soil by the Depth of the Lunar Rover Wheel Tracks. Solar System Research, 55, 285-308.

Breton S. et al. (2021) Terrain characteristics and selection of the Emirates Lunar Mission landing site. IAC-21,A3,IP,39,x66265, 72nd International Astronautical Congress (IAC), Dubai, United Arab Emirates, 25-29 October 2021.

Cahill, J. T. et al. (2014). The miniature radio frequency instrument's (Mini-RF) global observations of Earth's Moon. Icarus, 243, 173-190.

Carrier, W.D. (1973) Lunar soil grain size distribution. The Moon 6, 250-263.

Crawford, I. A., Anand, M., Barber, S., Cowley, A., Crites, S., Fa, W., ... & Tartèse, R. (2023). Lunar resources. Reviews in Mineralogy and Geochemistry, 89(1), 829-868.

Els, S., S. Almaeeini, & H. Almarzooqi (2021). The science system on-board the Emirates Lunar Mission's Rashid rover. In EGU General Assembly Conference Abstracts (pp. EGU21-12950).

Els, S., Overview of the ELM science investigations, submitted to this issue.

Flahaut, J., J. F. Blanchette-Guertin, C. Jilly, P. Sharma, A. Souchon, W. Van Westrenen, & D.A. Kring (2012). Identification and characterization of science-rich landing sites for lunar lander missions using integrated remote sensing observations. Advances in Space Research, 50(12), 1647-1665.

Flahaut, J. et al. (2020). Regions of interest (ROI) for future exploration missions to the lunar South Pole. Planetary and Space Science, 180, 104750.

Flahaut J. et al. (2021). Geology of the Lacus Somniorum region of the Moon, the Emirate Lunar Mission primary landing site. IAC-21,A3,2A,7,x64211, 72nd International Astronautical Congress (IAC), Dubai, United Arab Emirates, 25-29 October 2021.

Flahaut, J., van der Bogert, C. H., Crawford, I. A., & Vincent-Bonnieu, S. (2023a). Scientific perspectives on lunar exploration in Europe. npj Microgravity, 9(1), 50.

Flahaut J. et al. (2023b). Geology of Atlas crater, the Emirates lunar rover prime landing site, from combined remote sensing and in situ observations. The European Lunar Symposium, Padova, Italy, 27-29 June 2023.Fortezzo, C.M., P. D. Spudis, and S. L. Harrel (2020), Release of the Digital Unified Global Geologic Map of the Moon At 1:5,000,000- Scale, 51st Lunar and Planetary Science Conference, Houston, TX.,

Gaddis, L.R., M.I. Staid, J.A. Tyburczy, B.R. Hawke, N.E. Petro (2003). Compositional analyses of lunar pyroclastic deposits. Icarus 161 (2), 262–280. https://doi.org/ 10.1016/S0019-1035(02)00036-2.

Gaddis, L., B.R. Hawke, T. Giguere, S. Klem, J.O. Gustafson, S.J. Lawrence, J.D. Stopar (2012). Volcanism within floor-fractured Atlas crater. In: Lunar and Planetary Science Conference, Vol. 43.

Glotch, T. D., et al. (2011). The Mairan domes: Silicic volcanic constructs on the Moon. Geophysical Research Letters, 38(21).

Grolier, M. J. (1974). Geologic map of the Geminus Quadrangle of the Moon, USGS, IMAP 841.

Grumpe, A., Wöhler, C. (2014). Recovery of elevation from estimated gradient fields constrained by digital elevation maps of lower lateral resolution. ISPRS J. Photogrammetry and Remote Sensing 94, 37-54.

Hapke, B. (2012). Theory of Reflectance and Emittance Spectroscopy. 2nd ed., Cambridge University Press: Cambridge, UK.

Haruyama, J. et al. (2008). Global lunar-surface mapping experiment using the Lunar Imager/Spectrometer on SELENE. Earth, planets and space, 60(4), 243-255, doi:10.1186/BF03352788.

Heather, D.J. & S.K. Dunkin (2002). A stratigraphic study of southern Oceanus Procellarum using Clementine multispectral data. Planetary and Space Science, 50(14-15), pp.1299-1309.

Hiesinger, H., Jaumann, R., Neukum, G., & Head III, J. W. (2000). Ages of mare basalts on the lunar nearside. Journal of Geophysical Research: Planets, 105(E12), 29239-29275.

Hiesinger, H., Head III, J. W., Wolf, U., Jaumann, R., & Neukum, G. (2003). Ages and stratigraphy of mare basalts in oceanus procellarum, mare nubium, mare cognitum, and mare insularum. Journal of Geophysical Research: Planets, 108(E7).

Hiesinger, H., Head, J. W., Wolf, U., Jaumann, R., & Neukum, G. (2011). Ages and stratigraphy of lunar mare basalts: A synthesis. Recent Advances and Current Research Issues in Lunar Stratigraphy, 477, 1-51.

Horn, B. K. P. (1987). Height and gradient from shading. Int. J. Computer Vision 5, 37-75.

Hu, T., et al. (2020). Geological evolution of the Sinus Iridum basin. Planetary and Space Science, 194, 105134.

Joulaud, M. et al., Investigation of the regolith thickness and boulder density at the four Candidate Landing Sites of the Emirates Lunar Mission, submitted to this issue.

Jozwiak, L.M., J.W. Head, M.T. Zuber, D.E. Smith, G.A. Neumann (2012). Lunar floor fractured craters. Classification, distribution, origin and implications for magmatism and shallow crustal structure. J. Geophys. Res. Planets 117 (E11). https://doi.org/ 10.1029/2012JE004134.

Jozwiak, L.M., J.W. Head, L. Wilson (2015). Lunar floor-fractured craters as magmatic intrusions. Geometry, modes of emplacement, associated tectonic and volcanic features, and implications for gravity anomalies. Icarus 248, 424–447. https://doi. org/10.1016/j.icarus.2014.10.052.

Keller, J. W., Petro, N. E., & Vondrak, R. R. (2016). The Lunar Reconnaissance Orbiter Mission–Six years of science and exploration at the Moon. Icarus, 273, 2-24.

Kirk, R. E. (1987). I. Thermal Evolution of a Differentiated Ganymede and Implications for Surface Features. II. Hydromagnetic Constraints on Deep Zonal Flows in the Giant Planets. III. A Fast Finite Element Algorithm for Two-Dimensional Photoclinometry. Ph.D. Dissertation, California Institute of Technology, Pasadena, CA, USA.

Kramer, G. Y., Jaiswal, B., Hawke, B. R., Öhman, T., Giguere, T. A., & Johnson, K. (2015). The basalts of mare Frigoris. Journal of Geophysical Research: Planets, 120(10), 1646-1670.

Kring, D. A., & Durda, D. (2012). A global lunar landing site study to provide the scientific context for exploration of the Moon.

Lemelin, M., Blair, D. M., Roberts, C. E., Runyon, K. D., Nowka, D., & Kring, D. A. (2014). High-priority lunar landing sites for in situ and sample return studies of polar volatiles. Planetary and Space Science, 101, 149-161.

Lena, R., Wöhler, C., Phillips, J., & Chiocchetta, M. T. (2013). Lunar Domes, Springer Praxis Books, 174 pages, https://doi.org/10.1007/978-88-470-2637-7.

Liu, J., Zeng, X., Li, C., Ren, X., Yan, W., Tan, X., ... & Ouyang, Z. (2021). Landing site selection and overview of China's lunar landing missions. Space Science Reviews, 217, 1-25.

Losiak, A., D.E Wilhelms, C.J. Byrne, K.G. Thaisen, S.Z. Weider, T. Kohout, K. O'Sullivan, D.A. Kring, (2009). A new lunar impact crater database. In: Lunar and Planetary Science Conference, Vol. 40, 1532.

Lucey, P.G., D.T. Blewett & B.L. Jolliff (2000). Lunar iron and titanium abundance algorithms based on final processing of Clementine ultraviolet-visible images. Journal of Geophysical Research: Planets, 105(E8), 20297-20305.

Lucey, P., Korotev, R.L., Gillis, J.J., Taylor, L.A., Lawrence, D., Campbell, B.A., Elphic, R., Feldman, B., Hood, L.L., Hunten, D., Mendillo, M., Noble, S., Papike, J.J., Reedy, R.C., Lawson, S., Prettyman, T., Gasnault, O., Maurice, S. (2006) Understanding the lunar surface and Space-Moon interactions. Reviews in Mineralogy and Geochemistry 60, 83-219.

McKay, D.S., Heiken, G.H., Basu, A., Blanford, G., Simon, S., Reedy, R., French, B.M., Papike, J. (1991) The lunar regolith. In: Heiken, G.H., Vaniman, D., French, B.M.(Eds.), The Lunar Sourcebook: A User's Guide to the Moon. Cambridge University Press, pp. 285–356.

Michael G.G. & G. Neukum (2010). Planetary surface dating from crater size-frequency distribution measurements: Partial resurfacing events and statistical age uncertainty, Earth and Planetary Science Letters, 294 (3-4), 223-229.

Mitchell, J. K., Houston, W. N., Scott, R. F., Costes, N. C., Carrier III, W. D., & Bromwell, L. G. (1972). Mechanical properties of lunar soil: Density, porosity, cohesion and angle of internal friction. In Lunar and planetary science conference proceedings (Vol. 3, p. 3235).

NRC (National Research Council) (2007). The Scientific Context for Exploration of the Moon. Washington, DC: The National Academies Press. https://doi.org/10.17226/11954.

Qian, Y. Q., et al. (2018). Geology and scientific significance of the Rümker region in northern Oceanus Procellarum: China's Chang'E-5 landing region. Journal of Geophysical Research: Planets, 123(6), 1407-1430.

Qiao, L., L. Xiao, J. Zhao, Q. Huang & J. Haruyama (2014). Geological features and evolution history of Sinus Iridum, the Moon. Planetary and Space Science, 101, 37-52.

Robinson, M. S. et al. (2010). Lunar reconnaissance orbiter camera (LROC) instrument overview. Space science reviews, 150(1-4), 81-124.

Rutherford, M. J., Hess, P. C., Ryerson, F. J., Campbell, H. W., & Dick, P. A. (1976). The chemistry, origin and petrogenetic implications of lunar granite and monzonite. In Lunar and Planetary Science Conference Proceedings (Vol. 7, pp. 1723-1740).

Schaber, G. G. (1969). Geologic map of the Sinus Iridum quadrangle of the Moon. US Geological Survey Report, 602.

Schultz, P.H. (1976). Floor-fractured lunar craters. Earth Moon Planet. 15 (3), 241–273. https://doi.org/10.1007/BF00562240.

Scott, D.H. (1972). Geologic map of the Eudoxus Quadrangle of the Moon, USGS, IMAP 705.

Seddio, S. M., Jolliff, B. L., Korotev, R. L., & Zeigler, R. A. (2013). Petrology and geochemistry of lunar granite 12032, 366-19 and implications for lunar granite petrogenesis. American Mineralogist, 98(10), 1697-1713.

Shao, M., Chellappa, R., Simchony, T. (1991). Reconstructing a 3-D depth map from one or more images. CVGIP Image Understanding 53, 219-226.

Smith, D. E. et al. (2017). Summary of the results from the Lunar Orbiter Laser Altimeter after seven years in lunar orbit. Icarus, 283, 70-91.

Staid, M. I., Pieters, C. M., Besse, S., Boardman, J., Dhingra, D., Green, R., ... & Taylor, L. A. (2011). The mineralogy of late stage lunar volcanism as observed by the Moon Mineralogy Mapper on Chandrayaan-1. Journal of Geophysical Research: Planets, 116(E6).

Tang, Z., Liu, J., Wang, X., Ren, X., Chen, W., Yan, W., ... & Li, C. (2020). Physical and mechanical characteristics of lunar soil at the Chang'E-4 landing site. Geophysical Research Letters, 47(22), e2020GL089499.

Thiessen, F., Besse, S., Staid, M. I., & Hiesinger, H. (2014). Mapping lunar mare basalt units in mare Imbrium as observed with the Moon Mineralogy Mapper (M^3). Planetary and Space Science, 104, 244-252.

Thomson, B. J., Grosfils, E. B., Bussey, D. B. J., & Spudis, P. D. (2009). A new technique for estimating the thickness of mare basalts in Imbrium Basin. Geophysical Research Letters, 36(12).

Whitford-Stark, J. L., & Head III, J. W. (1980). Stratigraphy of Oceanus Procellarum basalts: Sources and styles of emplacement. Journal of Geophysical Research: Solid Earth, 85(B11), 6579-6609.

Wu, Y., et al. (2018). Geology, tectonism and composition of the northwest Imbrium region. Icarus, 303, 67-90.